



Full Length Article

Carbon nanofibers derived from bacterial cellulose: Surface modification by polydopamine and the use of ferrous ion as electrolyte additive for collaboratively increasing the supercapacitor performance

Zhong Jie Zhang^{a,*}, Xiang Ying Chen^{b,c}^a College of Chemistry & Chemical Engineering, Anhui University, Hefei 230601, Anhui, PR China^b Anhui Province Key Laboratory of Green Manufacturing of Power Battery, Tianneng Battery Group (Anhui Company), Jieshou 236500, Anhui, PR China^c School of Chemistry and Chemical Engineering, Hefei University of Technology, Hefei 230009, Anhui, PR China

ARTICLE INFO

Keywords:

Carbon nanofiber
Surface modification
Polydopamine
Redox additive
Supercapacitor

ABSTRACT

Carbon nanofibers (CNF) materials have been produced via the freeze-drying and carbonization processes, using commercial bacterial cellulose as carbon precursor. Then, the surface of CNF is modified by polydopamine (PDA), which largely deteriorates the surface area and pore volume but enhances the wettability. What's more, ferrous ion (Fe^{2+}) is introduced as redox additive, which has remarkably boosted the capacitive performance. The optimal sample delivers a high energy density of 10.07 Wh kg^{-1} at 1 kW kg^{-1} and large capacitance of 219 F g^{-1} at 10 A g^{-1} . Moreover, what attracts us is that the sample's increase fold (~ 10.17 times) is quite high, far exceeding the performance of common redox additives. Besides, it indicates favorable long-term cycling stability within 10,000 times (the capacitance retention up to 95%). The present strategy of PDA coating on carbon surface and use of redox additive pay the way to collaboratively boost the performance of supercapacitors.

1. Introduction

Based on a series of advantages, including high specific surface area (SSA), conductivity, stability, low cost, a wide range of sources, and a variety of allotrope, carbonaceous materials have become the superior choice of electrode materials for supercapacitors (SCs) [1,2]. Today, electrochemical double-layer capacitors (EDLCs) using carbon as the active material account for more than 80% of commercial production SCs [3]. Among the many types of carbon materials, currently the most widely used in the field of SCs are activated carbon, graphene and carbon nanotubes (CNTs). With respect to activated carbon, although the SSA is large (usually greater than $1000 \text{ m}^2 \text{ g}^{-1}$), the effective area that is electrochemically accessible does not linearly increase with SSA. More importantly, the pore structure of the carbon material produced by the traditional activation process is dominated by micropores, which is a big obstacle for SCs to obtain high performance [4,5]. The more hotspot is graphene and related 2D crystals and hybrid systems, demonstrating key features to meet emerging energy needs [6]. However, the disadvantage that graphene is easy to aggregate (π - π stacking) usually results in a significant reduction in its effective SSA, and the resistance to electron transport and ion transfer is greatly enhanced. Therefore, the graphene usually needs to be activated [7] or punched

[8], which increases the difficulty and cost of the operation. As for CNTs, it has excellent electrical conductivity (resulting in rapid electron transport) and structural stability [9]; however, the dense carbon structure also results in low SSA, which is obviously not good for SCs applications. As a response strategy, CNTs commonly need to be surface modified, activated or grafted [10]. So, is there a carbon material that has both 1D nanostructure and high SSA for SCs applications?

Obviously, carbon nanofibers (CNF) can meet this requirement to a certain extent. CNF are carbon materials with a cylindrical shape, similar to CNTs, but with different structure and texture characteristics. They can be divided into two types: highly graphitic CNF and lowly graphitic ones [11]. The most classic method for preparing well-defined CNF is to combine electrospinning with carbonization process, usually using polymer or hybrid as precursor [12–14]. However, the efficiency of synthesizing CNF using electrospinning technology is usually unfavorable, and how to achieve large-scale mass production has always been a challenge. In addition, it is notable that, as previously revealed, CNF with amorphous structures have larger SSA, which is more conducive to generating capacitive performances [15,16]. Therefore, the next research target is how to synthesize CNF, which can take into account both the amorphous structure and mass production feature, well realizing the efficient application in SCs. Excitingly, Yu and co-

* Corresponding author.

E-mail addresses: zhangzj06@ahu.edu.cn (Z.J. Zhang), chenxy@hfut.edu.cn (X.Y. Chen).<https://doi.org/10.1016/j.apsusc.2020.146252>

Received 3 February 2020; Received in revised form 24 March 2020; Accepted 28 March 2020

Available online 03 April 2020

0169-4332/ © 2020 Elsevier B.V. All rights reserved.

workers have made fruitful research achievements in this regard. Using bacterial cellulose (BC) as a raw material, controlled synthesis and mass production of CNF have been realized [17]. Through common freeze-drying and carbonization processes, the as-produced CNF usually exist in the form of aerogels, and they have been successfully used in many fields, including supercapacitors [18,19], superelastic and fatigue-resistant materials [20], ultralight, flexible, and fire-resistant materials [21], zinc-air battery [22].

In order to further improve the supercapacitor performance of CNF, it is usually compounded with other materials, which is a more feasible strategy. For instance, mixing CNF mats with up to 35 wt% MXene can form composite electrodes, delivering high areal capacitance, up to 205 mF cm⁻² at 50 mV s⁻¹, almost three times that of pure carbonized one (70 mF cm⁻² at 50 mV s⁻¹) [23]. CNF was firstly coated on porous silver network and then nitrogenated by NH₃ gas, in which silver improves the electron transport efficiency significantly and NH₃ can not only introduce nitrogen doping into CNF but also increase SSA [24]. Huang and Liu et al reported a novel N-doping method for CNF by introducing ZIF-8 (acting as nitrogen source and also template for pores) in the precursor, obtaining superior energy density of 31.04 Wh kg⁻¹ [25]. Furthermore, other different types of composite components have also been proposed for compounding with CNF, such as MnO₂ [26], graphene and CNTs [27], polyaniline [28] and carbon nanowhisker [29].

Herein, CNF materials were firstly produced via the freeze-drying and carbonization processes, using commercial bacterial cellulose as carbon precursor. Then, the surface of CNF was modified by polydopamine (PDA), which can somewhat improve the surface properties such as wettability, adhesion ability, and electronic conductivity. Thirdly, ferrous (Fe²⁺) ion as electrolyte additive was introduced, which can largely boost the capacitive performance mainly by the redox reaction. The capacitive performance was evaluated by three-electrode configuration and two-electrode configuration, respectively. The main purpose of this research is to propose a strategy to effectively improve the SCs performance of carbon materials, that is, the combination of PDA and electrolyte additive. The former can modify the surface of the carbon material to make it suitable for different types of electrolyte systems, while the latter can generate additional pseudo-capacitance through redox reactions, thereby greatly increasing the overall supercapacitor performance.

2. Experimental section

All chemicals are of analytical grade from Sinopharm Chemical Reagent Co., Ltd except for bacterial cellulose (BC) purchased from Hainan Yide Food Co., Ltd.

2.1. Typical procedure for synthesizing the CNF-blank sample

Firstly, the commercial BC was prepared into aerogel through freezing at 218.15 K for 48 h and vacuum drying overnight at 271.15 K. Next, the aerogel was heated to 1073.15 K for 2 h in N₂ flow, obtaining the **CNF-blank** sample.

2.2. Typical procedure for synthesizing the CNF-PDA sample

In a tris(hydroxymethyl)aminomethane hydrochloride solution (Tris-HCl, pH = 8.5, 1 L), 0.2 g dopamine was introduced and then stirred for 2 h at room temperature (RT); Subsequently, the above **CNF-blank** sample (0.2 g) was added. After stirring for 24 h at RT, the solid carbon sample was filtered, washed with deionized water and then dried at 353.15 K for 6 h under vacuum, yielding the **CNF-PDA** sample.

2.3. Typical procedure for synthesizing the mixed electrolyte

The mixed electrolytes were prepared by introducing ferrous

ammonium sulfate (FAS) into a 1 mol L⁻¹ H₂SO₄ solution under magnetic stirring at room temperature, keeping the FAS concentration as 0.25 mol L⁻¹, and the resulting samples are labeled as the **CNF-blank-Fe**, **CNF-PDA-Fe** samples, respectively.

2.4. Structure characterization

X-ray diffraction (XRD) pattern was obtained on a Rigaku D/MAX2500V with Cu K α radiation. Raman spectrum was recorded at ambient temperature on a Spex 1403 Raman spectrometer with an argon-ion laser at an excitation wavelength of 514.5 nm. Fourier transform infrared spectroscopy (FTIR) spectra of a sample in KBr pellet were recorded on a Thermo scientific Nicolet IS5 spectrometer. High-resolution transmission electron microscope (HRTEM) images, elemental mappings and EDAX spectrum were performed with a JEM-2100F unit. The specific surface area and pore structure of the carbon sample were determined by N₂ adsorption-desorption isotherms at 77 K (Quantachrome Autosorb-iQ). The specific surface area was calculated by the BET (Brunauer-Emmett-Teller) method. Pore size distribution was calculated by using a slit/cylindrical nonlocal density functional theory (NLDFT) model. X-ray photoelectron spectra (XPS) were obtained using a VG Instruments ESCALAB MK II X-ray photoelectron spectrometer with an excitation source of Al K α (1253.6 eV). The electrical conductivity was determined by measuring the impedance response of the test cell (1 × 1 cm²) using a ST2258C digital four-probe tester (Suzhou JingGe Electronic Co., Ltd) over the frequency range 1 Hz to 1 MHz. Contact angle tests were conducted by using a GR001PC130D contact angle tester (Jinzhitang, China).

2.5. Electrochemical measurements conducted in a three-electrode system

Typically, the carbon sample (80 wt%), graphite (15 wt%) and polytetrafluoroethylene (5 wt%) were mixed in ethanol. The mixed slurry (active carbon materials of 3 ~ 4 mg) was coated onto platinum net (~1 cm²) to prepare the working electrode, and the electrode was dried at 110 °C in an oven for 12 h. The three electrode system was executed in the prepared electrolyte (1 mol L⁻¹ H₂SO₄ solution) with a counter electrode of platinum foil (6 cm²) and a reference electrode of saturated calomel electrode (SCE). All tests were carried out on a CHI 760E (ChenHua Instruments Co. Ltd., Shanghai). The electrochemical performances of the samples were evaluated by cyclic voltammetry (CV), galvanostatic charge-discharge (GCD), and electrochemical impedance spectroscopy (EIS) techniques. The EIS measurements were carried out in the frequency range from 100 kHz to 0.01 Hz at open circuit potential with an ac perturbation of 5 mV.

Specific capacitances derived from galvanostatic tests can be calculated from the equation:

$$C = \frac{I dt}{m dU} \quad (1)$$

where C (F g⁻¹) is the specific capacitance; I (A) is the discharge current; t (s) is the discharge time; U (V) is the potential; and m (g) is the mass of active materials loaded in working electrode.

2.6. Electrochemical measurements conducted in a two-electrode system

The electrochemical experiments in two-electrode system were performed in a CR2032 coin-type cell. The carbon electrode was used as the working electrode and another carbon electrode with the same mass of active material was used as the counter electrode. A glassfiber membrane was used as the separator for the symmetric supercapacitor. Note that the mass of active carbon materials on each electrode is 1 ~ 2 mg.

Specific capacitances derived from galvanostatic tests can be calculated from the equation:

$$C = \frac{2I dt}{m \Delta U} \quad (2)$$

where I (A) is the constant current; m (g) is the mass of active material loaded on the single electrode; U is the voltage window (V); C ($F g^{-1}$) is the specific capacitance.

Specific energy density (E) and specific power density (P) derived from galvanostatic tests can be calculated from the equations:

$$E = \frac{1}{3.6} \times \frac{1}{8} \times C \Delta U^2 \quad (3)$$

$$P = \frac{3600E}{\Delta t} \quad (4)$$

E ($Wh kg^{-1}$) is the energy density; C ($F g^{-1}$) is the specific capacitance; U (V) is the potential; and P ($W kg^{-1}$) is the power density and t (s) is the discharge time.

3. Results and discussion

As we all know, BC is a valuable commodity for microbial polysaccharides with the formula of $(C_6H_{10}O_5)_n$ produced by certain types of bacteria. Due to its many useful properties and low cost production over a wide range, BC is being used for a wide variety of commercial applications including textiles, cosmetics, and food products, as well as medical applications [30]. Especially worth mentioning is that BC is a kind of highly uniaxially oriented nanofibers, which is composed of a network of ultrafine cellulose, so that it has many other unique applications such as energy storage, mechanics, and composite materials [31,32]. In this work, we firstly used BC as a precursor to prepare CNF materials through freeze-drying and carbonization processes. Subsequently, the surface of CNFs was modified by PDA, and the whole synthesis process is shown in Fig. 1a. In fact, BC itself has very typical 1D structural characteristics [33,34], whether or not freeze-dried. The freeze-drying process can effectively maintain the 3D spatial structure of the BC gel (especially the microscopic 1D nanostructure as building block); then, through a direct high-temperature carbonization strategy, 3D carbon aerogel material can be synthesized (constructed with fine 1D CNF units). On the other hand, PDA and its derivative materials

have been striking for promising applications in energy, environmental, and biomedical fields owing to wide and excellent biocompatibility [35]. What's more, PDA owns many functional groups such as catechol, amine, and imine, which can serve as effective platform for non- or covalent modification with other substances such as carbon materials [36]. Herein, the as-produced CNF materials were further coated/modified with PDA by an oxidative self-polymerization procedure (although there is still a lot of uncertainty in its essential structure) [37], which is anticipated to largely adjust the surface functionality of CNF including wettability, adhesion ability, and electronic conductivity. Of course, the functional groups from PDA can also generate interactions with the subsequent electrolyte additive of Fe^{2+} .

Next, the CNF-blank and CNF-PDA samples (before or after PDA coating) were characterized by several techniques. Fig. 1b shows the XRD patterns with 2 theta scope from 5 to 90°, in which there exists one broad but low-intensity diffraction peak centered at 23.4° (far below the one of 26.6° for standard graphite). This is basically consistent with the XRD data of conventional activated carbon, which means that the crystallinity of the sample is low, presenting an amorphous state [38]. In addition, this kind of amorphous feature toward the CNF-blank and CNF-PDA samples were further confirmed by Raman spectra, as displayed in Fig. 1c. The two bands located at 1342.0 and 1596.4 are indexed as D band and G band, respectively, representative symbol for carbon materials. The former D band indicates the disordered graphitic lattice (A_{1g} symmetry), whilst the latter G band reveals the ideal one with E_{2g} symmetry [39]. Obviously, the coexistence of D and G band indicates the amorphous structure of carbon material, and moreover, the 2D band is relative smooth (not prominent), which also indicates the low-graphitization degree [40]. FTIR was also used to detect the presence of PDA on CNF surfaces. However, unfortunately, the FTIR results are almost undetectable perhaps due to the small amount of PDA adherent on the CNF surface. As a result, only in the range of 1200–1620 cm^{-1} , the appearance of a small number of absorption peaks occurs in Fig. 1d, which approximately correspond to the PDA molecules [41,42]. Later, we will use more accurate XPS for PDA detection. Furthermore, the morphology of the CNF-PDA sample synthesized in this experiment was roughly detected by HRTEM tool. As shown in Fig. 1e, the sample is composed of a large number of 1D

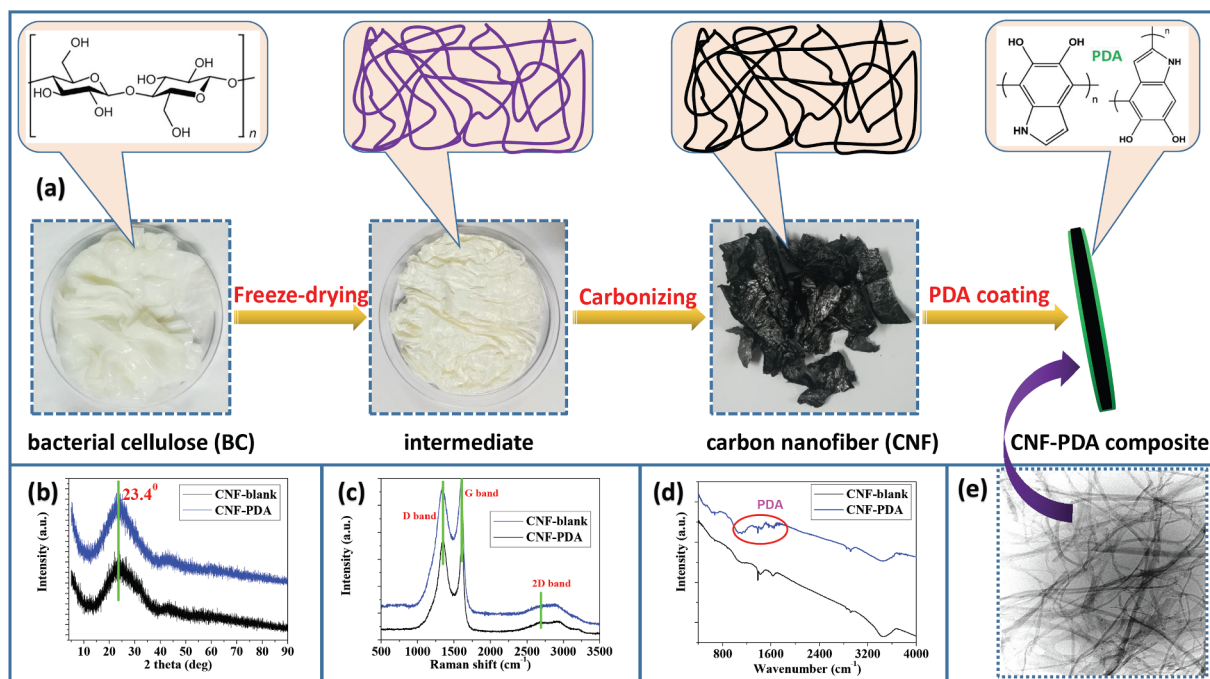


Fig. 1. (a) Schematic drawing for producing CNF and CNF-PDA composite; the CNF-blank and CNF-PDA samples of (b) XRD patterns; (c) Raman spectra; (d) FTIR spectra and (e) HRTEM image of the CNF-PDA sample.

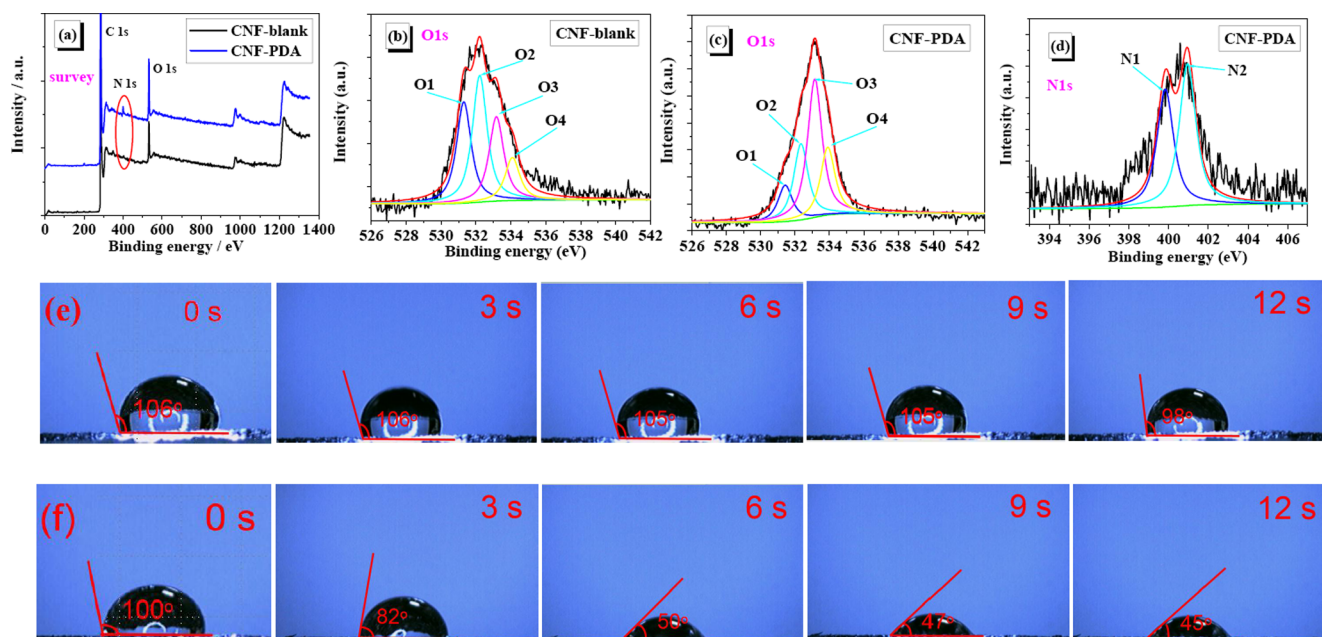


Fig. 2. XPS of the CNF-blank and CNF-PDA samples: (a) Survey spectra; (b, c) O1s; (d) N1s; as well as water contact angle over time (e, f).

nanofibrous materials with a large aspect ratio and intertwined and curled, which is basically consistent with the appearance characteristics of the sample (fluffy and porous state). This form of CNF also accords with the previous reports of many documents. As for more detailed structural inspection and description, it will be carried out in the subsequent HRTEM section.

As described previously, dopamine can be converted to polydopamine by oxidative self-polymerization process. However, the amount of PDA on the surface of the carbon material is very small, and the thickness is usually only a few nanometers [43,44]. And this scale just fits the detection range of the XPS method, which can quantitatively give information about the elemental composition and chemical valence/state of the PDA coating. Fig. 2a indicates the XPS survey of the CNF-blank and CNF-PDA samples with the binding energy of 0 ~ 1400 eV. Obviously, the CNF-PDA sample is composed of C, N, and O elements, while the CNF-blank sample contains only C and O. Next, we will perform a scientific fitting process on the representative O1s and N1s. With the help of XPSPEAK software, the O1s peaks of these two samples can be fitted into four secondary peaks [45,46], as shown in Fig. 2b, c. But their molar percentages are quite different in Table 1, which is obviously caused by the coating of the PDA on the surface of the CNF material. As for the N1s peak caused by PDA, it can be fitted to two distinct secondary peaks, as depicted in Fig. 2d. In details, the group of $-\text{NH}_2$ comes from dopamine, whereas the $-\text{N}=\text{}$ and/or $-\text{NH}$ groups should be assigned to dopamine and its intermediate derivatives

Table 1

The XPS data and molar percentage of C, O and N species of samples.

Element	Binding energy (eV)	Assignment	Molar percentage (%)	
			CNF-blank	CNF-PDA
O 1s	531.3	C=O (carboxyl)	28.50	11.40
O 1s	532.2	C=O (ester, amide)	35.65	23.88
O 1s	533.2	C—OH	23.76	43.42
O 1s	534.1	O=C—O	12.09	21.30
N 1s	399.5	$-\text{N}=\text{}$ / $-\text{NH}$	/	14.28
N 1s	401.3	$-\text{NH}_2$	/	85.72
Elemental composition:				
C			93.05	87.40
O			6.95	9.55
N			/	3.05

[41], fully considering the complexity and uncertainty in the process of PDA polymerization [47].

The degree of hydrophilicity of the carbon material directly determines the performance and efficiency of the electrolyte in and out of the electrode. Therefore, ameliorating the hydrophilicity of the surface of the carbon material is an important way to improve the performance of the supercapacitor. Taking graphene fibers as example, introducing cellulose nanocrystal [48] or treating with KOH [49,50] can largely enhance the hydrophilicity. For PDA, it is well known to use its super hydrophilicity to improve performance. For example, simply dipping PDA makes the PE surfaces hydrophilic and thus enhances the power capabilities remarkably [51]; Lee reported surface-adherent PDA films onto a wide range of inorganic and organic materials [52]. Herein, Fig. 2e presents the water contact angle from 106 to 98° over 12 s concerning the CNF-blank sample, evidently revealing the feature of hydrophobicity; on the contrary, the CNF-PDA sample exhibits hydrophilic surface in that the contact angle quickly decrease from 100 to 45° within the same time. Consequently, the PDA coating on carbon materials has indeed exerted crucial role on the elevation of hydrophilicity, and apparently, this will be very beneficial to speed up the efficiency of the electrolyte in and out of the carbon electrode, thereby improving the electrochemical performance.

As expected, the CNF sample is composed of a large number of nanofibers (the yield of the 1D structure is almost 100%). As shown in Fig. 3a,b, these nanofibers of the CNF-blank sample exhibit a typical curl shape (entangled but independent of each other) with a large aspect ratio. In order to study the degree of crystallization of the CNF-blank sample, they need to be further enlarged. As a result, Fig. 3c shows two separated carbon nanofibers. Therein, they can be judged to exhibit typical amorphous features, especially combined with a partial enlarged picture (shown in the inset), and the lattice fringes are short-range disordered. These amorphous features are consistent with the XRD and Raman test results mentioned earlier. The composition and distribution of various elements in these carbon nanofibers can be detected using in-situ EDAX spectroscopy. As shown in Fig. 3d, the CNF-blank sample mainly contains carbon and oxygen (determinable from the color of the element), and the content of carbon is significantly higher than that of oxygen (determinable from the depth of the element color). In addition, it is clear that the results of this EDAX spectrum are basically compatible with the aforementioned XPS results. As for the

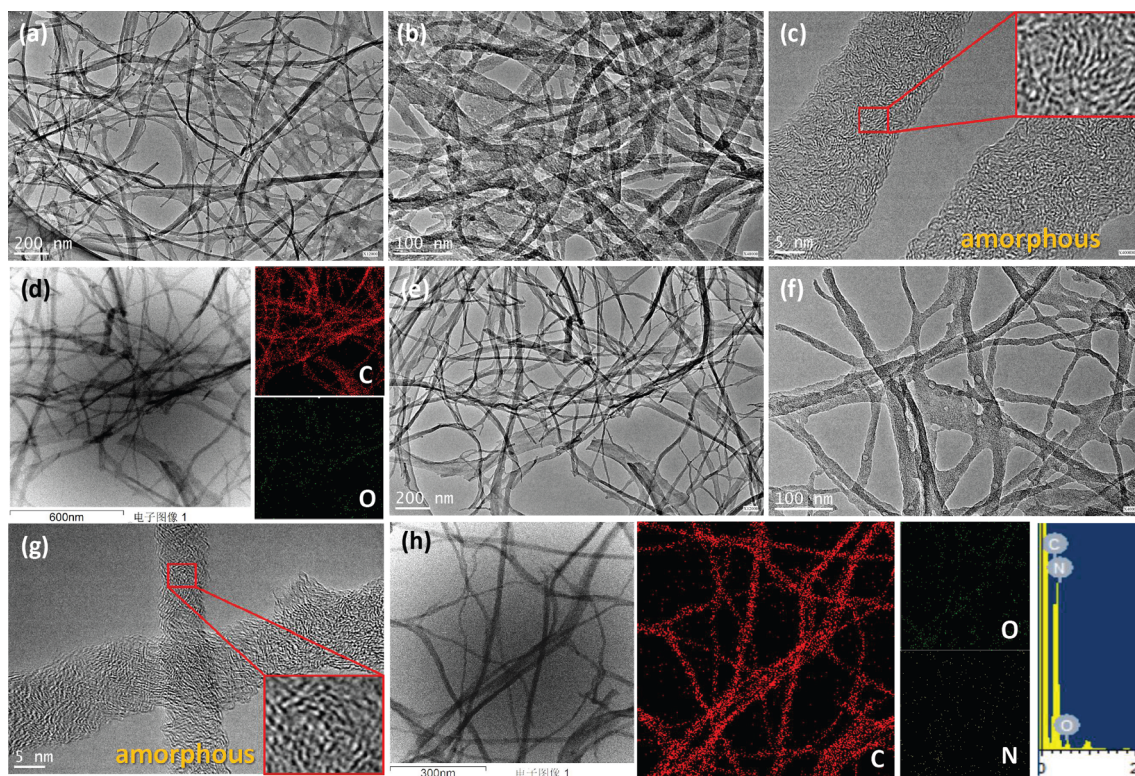


Fig. 3. HRTEM images and elemental mapping together with EDAX spectrum: (a-d) The CNF-blank and (e-h) CNF-PDA samples.

CNF-PDA sample, the overall HRTEM results are basically similar to that of the CNF-blank sample, which also shows 1D nanometer amorphous structure with a large aspect ratio; the distribution of the three constituent elements C, N, and O also meets expectations (N content is nearly undetectable owing to its low content), which is also in line with the previous XPS results.

Porosity (mainly including BET surface area, pore volume and PSD) is a very critical parameter for carbon materials, which can strongly affect the efficiency and rate of electrolyte in and out of the electrode, and then determine the performance of the entire supercapacitor. Among them, PSD generally needs to have a well-defined hierarchical structure (that is, micropores, meso/macropores should have both), quite favorable for the electrolyte wetting and rapid ionic motions especially at high current loads. N_2 adsorption-desorption isotherms toward the CNF-blank and CNF-PDA samples are depicted in Fig. 4a. Both isotherms have a short steep adsorption in the low pressure region (~ 0), and on the other side, there exists obvious hysteresis loops in the medium and high pressure region (0.45 \sim 1.0), which indicate that both samples have micropores and mesopores / macropore [38,53]. This kind of hierarchical pore structure can also be verified by PSD results, as shown in Fig. 4b. They all have PSD peaks in the scope smaller or greater than 2 nm. However, compared to the CNF-PDA sample, the PSD peak of the CNF-blank sample is sharper and more pronounced; this is mainly due to the PDA coating on the surface of the carbon material (blocking the pores to a certain extent).

The difference between isotherm and PSD mentioned above is also reflected in the data of BET specific surface area and pore volume. Resultantly, the BET surface areas of the CNF-blank and CNF-PDA samples are of 464 and 191 $m^2 g^{-1}$, and the pore volumes of 0.63 and 0.43 $cm^3 g^{-1}$, respectively. Obviously, the introduction of PDA on the surface has caused a significant decrease in the porosity of the carbon-PDA composite. In the meantime, the proportion of BET surface areas for micropore and meso/macropore are further calculated, as given in Fig. 4d. It is clearly discerned that incorporating PDA onto the carbon surface has resulted in the increase of micropore, also accompanied

with the decrease of meso/macropore. This indicates that the PDA is mainly filled in the gaps between the carbon material blocks and less enters the interior of the micropores (this is partially related to the strong adhesion, large molecular size of the PDA itself etc).

Next, the electrochemical performance of pristine CNF samples before and after PDA coating as well as the ones combined with electrolyte additive of Fe^{2+} were tested in a three-electrode configuration, using 1 mol L^{-1} H_2SO_4 solution as aqueous electrolyte. Fig. 5a indicates the contrastive CV curves at a fixed scan rate of 10 $mV s^{-1}$ towards the CNF-blank, CNF-PDA, CNF-blank-Fe, CNF-PDA-Fe samples. For the CNF-blank sample, the CV curve basically shows a rectangular outline, which indicates that its EDLCs contribution is dominant; for the other three samples, their CV curves are more seriously deviated from the rectangle, which means that the contribution from pseudo-capacitance is growing (the specific mechanism for the generation of pseudo-capacitance will be illustrated in the following section). In particular, after introducing a certain concentration of Fe^{2+} ions into the H_2SO_4 electrolyte, a pair of relatively distinct and symmetrical redox peaks can be generated in the range of 0.4–0.8 V, which basically accords with our previous reports [54]. Besides, the peak separation between anodic and cathodic peaks (ΔE_p) is an indicator of electron transfer kinetics or electrochemical reversibility. Generally speaking, for an electrochemically reversible reaction, electrons are transferred to the electrode faster than voltammetry scans (the ideal ΔE_p is close to 0 mV) [55]. Herein, the CNF-blank-Fe, CNF-PDA-Fe samples show the ΔE_p as 0.20 and 0.24 V, respectively, when designated at 10 $mV s^{-1}$, hereby indicating the irreversible feature during the redox process.

Similar irreversible phenomena also appear on the GCD curve at 10 $A g^{-1}$. For the CNF-blank sample, its GCD curve basically remains a regular triangle; the other three samples are greatly switched from the standard triangle. Especially for the CNF-blank-Fe, CNF-PDA-Fe samples, a significant redox plateau appears on their GCD curves between 0.4 and 0.8 V, which is basically consistent with the position of the redox peak on the CV curve. Furthermore, specific capacitances (Cs) at different current densities were calculated, as given in Fig. 5c. In

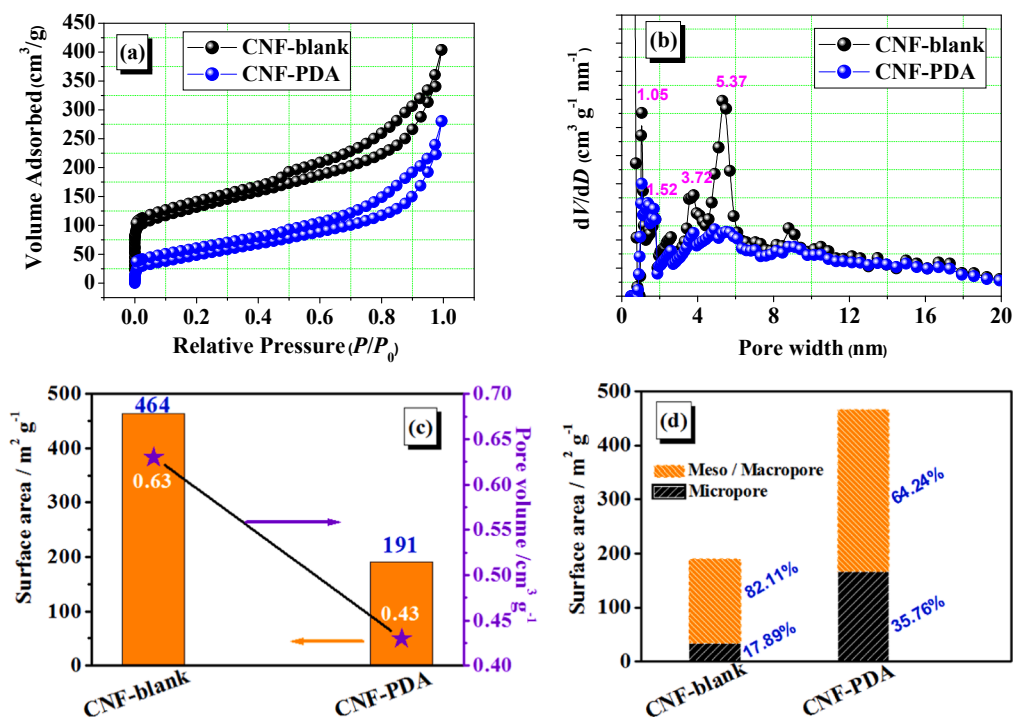


Fig. 4. The CNF-blank and CNF-PDA samples: (a) N₂ adsorption-desorption isotherms; (b) PSD curves; (c) BET surface areas and pore volumes; (d) Proportion of BET surface areas for micropore and meso/macropore.

general, the specific capacitance of the CNF-blank sample is poor, and PDA surface coating can improve it to some extent; in addition, it is interesting to note that the introduction of an appropriate amount of Fe²⁺ in the H₂SO₄ electrolyte can significantly improve the specific capacitance. For instance, at a current density of 10 A g⁻¹, Cs of the

CNF-blank, CNF-PDA samples are of 26, 64F g⁻¹, whereas those of the CNF-blank-Fe, CNF-PDA-Fe samples are increased up to 183, 260F g⁻¹, respectively. With respect to Nyquist plot, it shows the frequency response of the electrode/electrolyte system and is a plot of the imaginary component (Z'') versus real component (Z') of the impedance. In

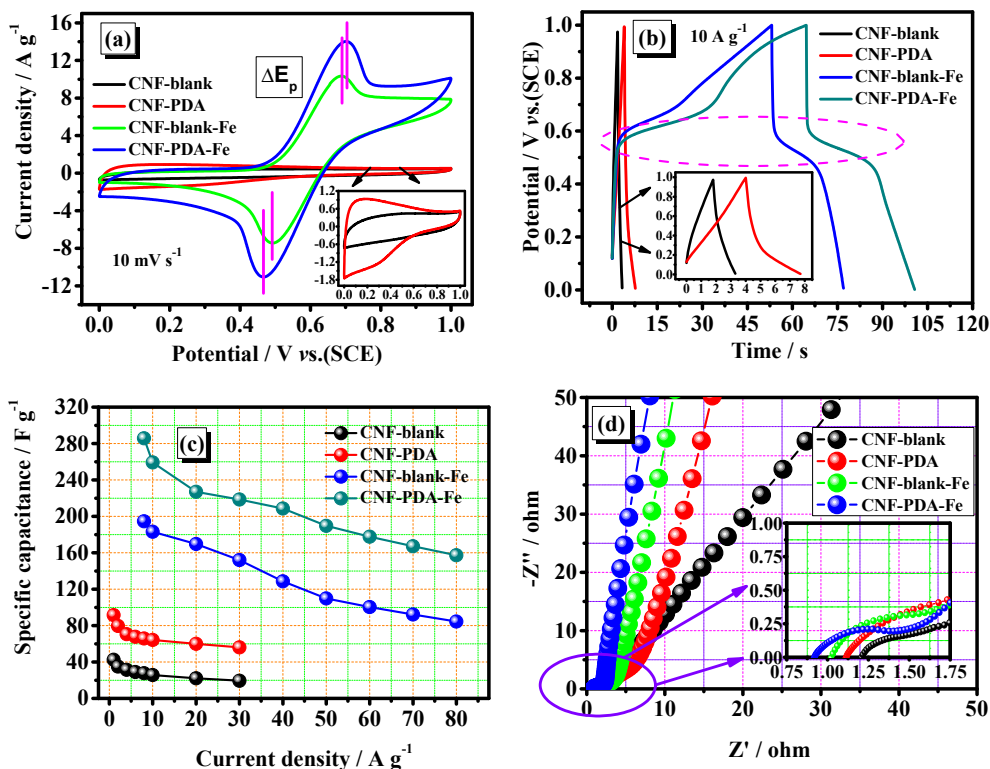


Fig. 5. The CNF-blank, CNF-PDA, CNF-blank-Fe, CNF-PDA-Fe samples when tested in a three-electrode configuration using 1 mol L⁻¹ H₂SO₄ solution as aqueous electrolyte: (a) CV curves at 10 mV s⁻¹; (b) GCD curves at 10 A g⁻¹; (c) Specific capacitances at different current densities; (d) Nyquist plots.

Fig. 5d, by carefully observing the Nyquist magnification curve in the high frequency region, it can be found that there is a slight difference between the intersection of the curves of the four samples (ie, the intercept). The **CNF-PDA-Fe** sample has the smallest intercept and the **CNF-blank** sample has the largest one. Moreover, the order of the intercepts of these samples is compatible with the electrochemical change trend described above. From the intercept point of view, the electrode resistance of sample is the smallest, while the **CNF-blank** sample is the largest [56]. This trend can also be verified in the low-frequency curve. The curve of the **CNF-blank** sample deviates the most from the vertical line, whilst the sample of **CNF-PDA-Fe** is the smallest in that as is well known, the cell corresponds more closely to an ideal capacitor the more vertical the curve [57].

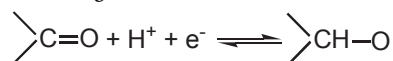
Furthermore, after the redox additive is added to the electrolyte, it will pass through a series of kinetic steps such as diffusion in the bulk phase, surface reaction of the electrode material, and diffusion in the void etc [58]. Therefore, it is important to estimate the key control steps of the additive through electrode kinetics. In general, the scan rate at which the current response is applied will vary depending on whether the redox reaction is diffusion controlled or surface controlled. For redox reactions confined by semi-linear diffusion, the current response changes with $v^{1/2}$; on the other hand, for a capacitive process, the current varies directly with v [59,60]. For the present **CNF-blank-Fe**, **CNF-PDA-Fe** samples, both of them exhibit the current response varying with $v^{1/2}$ in the scope of 10–80 mV s⁻¹, clearly evincing the diffusion-controlled manner of Fe²⁺ ions. Even in the absence of PDA, the interaction between the electrolyte additive of Fe²⁺ and hierarchical carbon material are diffusion-controlled [54], which indicates that the presence of PDA cannot change the kinetic characteristics of Fe²⁺ ions.

In fact, most of the kinetic processes of electrolyte additives are diffusion controlled, which is mainly because the migration rate of these molecules in the bulk phase is quite fast, while in the microporous and mesoporous structure of carbon electrode, it becomes much slower. These examples typically include hydroquinone (HQ) and methylene blue (MB) in PVA-H₂SO₄ gel polymer electrolytes [34], 1, 4-dihydroxyanthraquinone (DQ) and hydroquinone (HQ) in H₂SO₄ electrolyte [61], Na₂MoO₄ and KI in H₂SO₄ electrolyte [62], phosphotungstic acid (PTA) and K₃[Fe(CN)₆] in H₂SO₄ electrolyte [63], anthraquinone-2,7-disulphonate (AQDS) and K₄Fe(CN)₆ in the neutral medium of KNO₃ [64]. However, if the additives react, compound or graft with the surface functionality of the carbon electrode material, they will be bound to the surface of the carbon material, so that the kinetics of surface control occurs. For example, the mediator of flavin adenine dinucleotide (FAD) and polymer were electrochemically deposited with a poly (3,4-ethylenedioxythiophene) (PEDOT) as a composite on a glass carbon electrode (GCE). And therefore, the redox reaction of FAD is surface controlled [65]; Similarly, anthraquinone (AQ) also complies with kinetics of surface control in that these molecules can functionalize with hierarchically porous graphitic carbon fibers (HPGCFs) via π - π stacking interactions [66].

In order to distinguish and determine the ratio and contribution of EDLC and pseudo-capacitance to the total capacitance, the Trasatti method was adopted because it has been proven to be an effective strategy [67]. Herein, in the scope of 10 ~ 100 mV s⁻¹, by linear fitting of the reciprocal curve of C (C⁻¹) against square root of scan rate ($v^{0.5}$), it yields total specific capacitance, as shown in Fig. 7a; on the other side, similar linear fitting of the specific capacitance (C) against the reciprocal of square root of the scan rate ($v^{-0.5}$) results in the capacitance for EDLCs, as depicted in Fig. 7b. Then, by subtracting EDLCs from total specific capacitances, the pseudo-capacitances are achieved [40,68]. As a consequence, the contribution of EDLC and pseudo-capacitance concerning these four samples can be further calculated, as displayed in Fig. 7c. The oxygen-containing functional groups (as shown in Table 1) on the surface of the **CNF-blank** sample can produce pseudo-capacitance; furthermore, the incremental pseudo-capacitance

of the **CNF-PDA** sample is derived from amino-functional redox reaction of PDA coating. Obviously, the incorporation of Fe²⁺ as redox additive into H₂SO₄ solution has generated more contribution of pseudo-capacitance for the cases of the **CNF-blank-Fe**, **CNF-PDA-Fe** samples, compared to those of the oxygen-/amino-functionalities on the carbon surface.

In present work, apart from EDLCs stemmed from porous carbon materials, there are several other types of pseudo-capacitances. Studies have shown that oxygen-containing functional groups can largely improve the wettability of carbon electrode materials, the utilization of pores, and also generate a pseudocapacitive reaction. Moreover, in the acid electrolyte, the electrons on the oxygen functional group are attracted by H₃O⁺, which results in the separation of positive and negative charges, thereby causing the redox reaction to occur [69]. Different types of oxygen-containing functional groups can undergo different redox reactions. Taking carbonyl as an example, in an acid electrolyte, the following reactions can occur [70]:



In addition, it is interesting that PDA can not only adjust the wettability and adhesion of carbon materials, but also expect to generate a pseudocapacitive reaction in the electrolyte, in particular considering its own amino and hydroxyl functional groups. As a matter of fact, PDA can indeed undergo a series of pH-dependent pseudocapacitive reactions. In an acidic system, the amino group in the PDA molecule is protonated, and the two hydroxyl groups can reversibly form carbonyl groups through the gain and loss of two protons and two electrons [71], as shown in Fig. 7d. A similar reaction mechanism has been verified in the *p*-aminophenol system [72]. Besides, for the case of Fe²⁺ ions, the corresponding electrochemical reaction mechanisms are also shown in Fig. 7d. During the charging process, Fe²⁺ is oxidized to Fe³⁺, losing one electron simultaneously in the positive electrode. In the negative electrode, the active carbon atoms on the carbon surface can reduce Fe³⁺ to Fe²⁺ and also form a complex state through electrostatic adsorption [54,73]. As a result, additional Faradaic pseudo-capacitance can be generated. As for the discharge process, the mechanism involved is exactly the opposite. Of course, it is also possible that there exists spatial charge storage mechanism based on counterion effect from Fe²⁺ ions bridged by oxygen/amino groups and confined into porous carbon matrix [74].

Compared to the three-electrode, the two-electrode system can provide a more accurate and reliable electrochemical test result [57], so we further performed two-electrode test on these four samples. For convenience, we directly gave the specific capacitance data with different current densities, as shown in Fig. 8a. Obviously, the change law of Cs in the two-electrode system is similar to that of the three-electrode system (in Fig. 5c), but the value is reduced, which is usually caused by the reduction of the wetting efficiency between the electrolyte, additives and carbon electrode materials in the two-electrode system. For instance, at a current density of 10 A g⁻¹, Cs of the **CNF-blank**, **CNF-PDA** samples are of 14 and 42F g⁻¹, whereas those of the **CNF-blank-Fe**, **CNF-PDA-Fe** samples reach up to 128 and 219F g⁻¹, respectively. Moreover, using these Cs, Ragone plots showing the function of energy density over power density are obtained, as displayed in Fig. 8b. It is apparent that the energy densities of the samples have been greatly improved by the incorporation of Fe²⁺ ions. At a power density of 1 kW kg⁻¹, the resulting energy densities of the **CNF-blank**, **CNF-PDA** samples are 0.99 and 2.14 Wh kg⁻¹; and those of the **CNF-blank-Fe**, **CNF-PDA-Fe** samples are boosted to be 6.96 and 10.07 Wh kg⁻¹, respectively. In other words, with the collaborative promotion of PDA coating and Fe²⁺, the energy density of CNF materials has increased by 10.17 times. In addition, cycling stability is one of the important parameters of supercapacitors. Fig. 8c indicates the long-term cycling stability within 10,000 times, in which the **CNF-PDA-Fe** sample

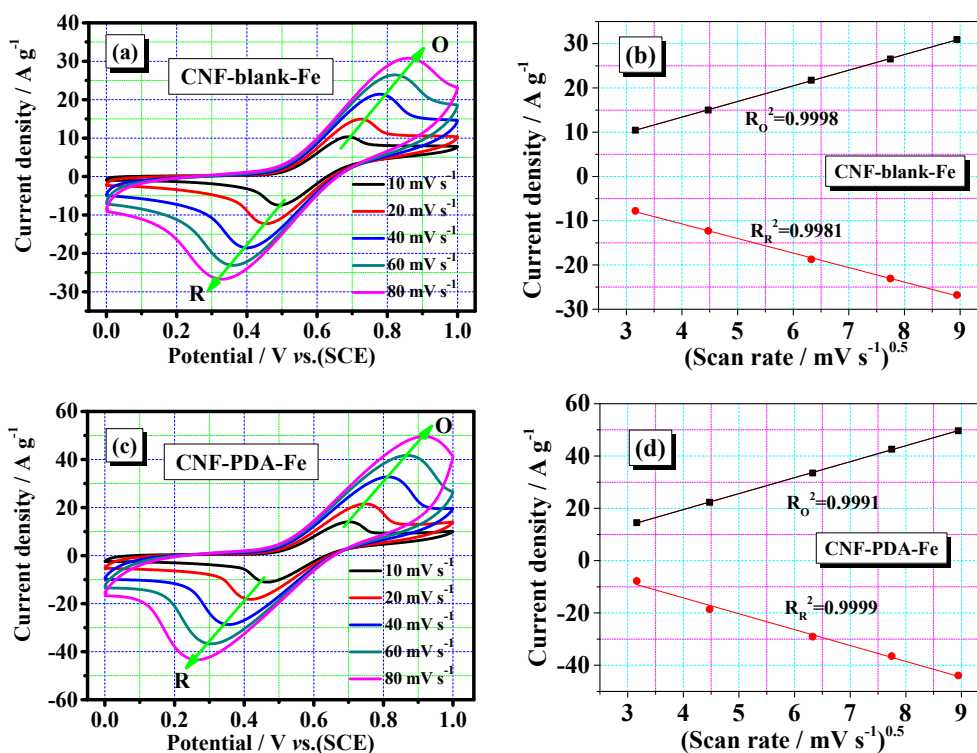


Fig. 6. The CNF-blank-Fe, CNF-PDA-Fe samples when tested in a three-electrode configuration using 1 mol L⁻¹ H₂SO₄ solution as aqueous electrolyte: (a, c) CV curves at various scan rates; (b, d) Relationship between peak intensity and scan rate.

delivers the best cycling performance (the Cs retention up to 95%) and yet that of the CNF-blank sample's is worst (~79%).

In a two-electrode configuration, Nyquist plots of these samples are displayed in Fig. 9a, whose trend is primarily compatible to those in Fig. 5d. In virtue of the flat arc length in the high frequency region, it can be judged that the electrolyte resistance of the CNF-blank sample is the largest, whilst the CNF-PDA-Fe sample is the smallest. Also, the low and non-vertical line at intermediate frequency (so-called Warburg plot) reveals the existence of diffuse layer resistance [56], well according with kinetics results in Fig. 6. Furthermore, the dependence of phase angle on the frequency as Bode plot is estimated and presented in Fig. 9b. As we know, the characteristic frequency at which the phase angle reaches 45° is knee frequency (f_0), where the capacitive and the resistive impedances are equal [75]. Beyond this point, the supercapacitor shows more resistive behavior at higher frequency. The relaxation time ($\tau_0 = 1/f_0$) indicates the minimum time for discharging all the energy from the device with an efficiency of greater than 50%. As a result, the relaxation time of the CNF-blank, CNF-PDA, CNF-blank-Fe, CNF-PDA-Fe samples is found to be 17.9, 8.3, 5.3, and 2.8 s, respectively. That is to say, the CNF-PDA-Fe sample exhibits the highest rate capability (ie, the lowest τ_0).

Besides, the simultaneous observation of the potential distribution of the positive and negative electrodes allows for further clarification of the Faradaic reaction mechanism [76]. Fig. 9c shows the GCD curves of the CNF-blank-Fe sample (cell voltage, left Y-axis) and the corresponding potential distribution across the positive and negative electrodes (right Y-axis). The potential on the positive electrode is distributed in the range of 0 to -0.6 V, which is basically triangular; while the potential on the negative electrode is distributed in the range of -0.3 to -0.7 V, which severely deviates from the triangle. This shows that the pseudocapacitive reaction produced by Fe²⁺ occurs on the negative electrode, just like that of KI additive in H₂SO₄ [77]. As for the CNF-PDA-Fe sample, similar results also appear in Fig. 9d.

For the performance of the samples in this experiment, we also compared with typical literature results, as shown in Table 2. Three

indicators are examined, including Cs, energy density, and its increase fold. Taking the best CNF-PDA-Fe sample as an example, it can still maintain a specific capacitance of 219F g⁻¹ at a current density of up to 10 A g⁻¹, which indicates that the sample's rate capability is quite outstanding; however, the energy density is small as 10.07 Wh kg⁻¹ when tested at a power density of 1 kW kg⁻¹, which is obviously related to its smaller BET surface area (191 m² g⁻¹) and lower pore (0.43 cm³ g⁻¹). In other words, the specific capacitance and energy density per unit volume of the sample would be rather large. However, what attracts us is that the sample's increase fold (10.17 times) is quite high, far exceeding the performance of common redox additives [19,61,68,78–83]. This should be attributed to the PDA coating on the surface of the carbon material, which can significantly regulate the wettability, electrical conductivity, and pseudo-capacitance as well, somewhat similar to the case of Px-MWCNT/PANI nanocomposite collaboratively with HQ [84]. It can be thus inferred that the surface coating of PDA can be used as a universal strategy to achieve the modification and improvement of electrode materials.

4. Conclusions

In summary, we firstly demonstrate a freeze-drying and carbonization process for largely producing CNF materials, using commercial bacterial cellulose as raw materials. Then, PDA is coated on the surface of CNF sample; thirdly, Fe²⁺ ions are incorporated into H₂SO₄ electrolyte as redox additive. The points worthy of our attention in this work are as follows:

- (1) PDA coating on the surface of the CNF material, can significantly reduce the porosity but ameliorate the wettability;
- (2) PDA can not only generate pseudo-capacitance by itself, but also cooperate with Fe²⁺ to significantly improve the overall electrochemical performance;
- (3) Regardless of the presence or absence of PDA, the Fe²⁺ reaction kinetics is diffusion-controlled during the redox process;

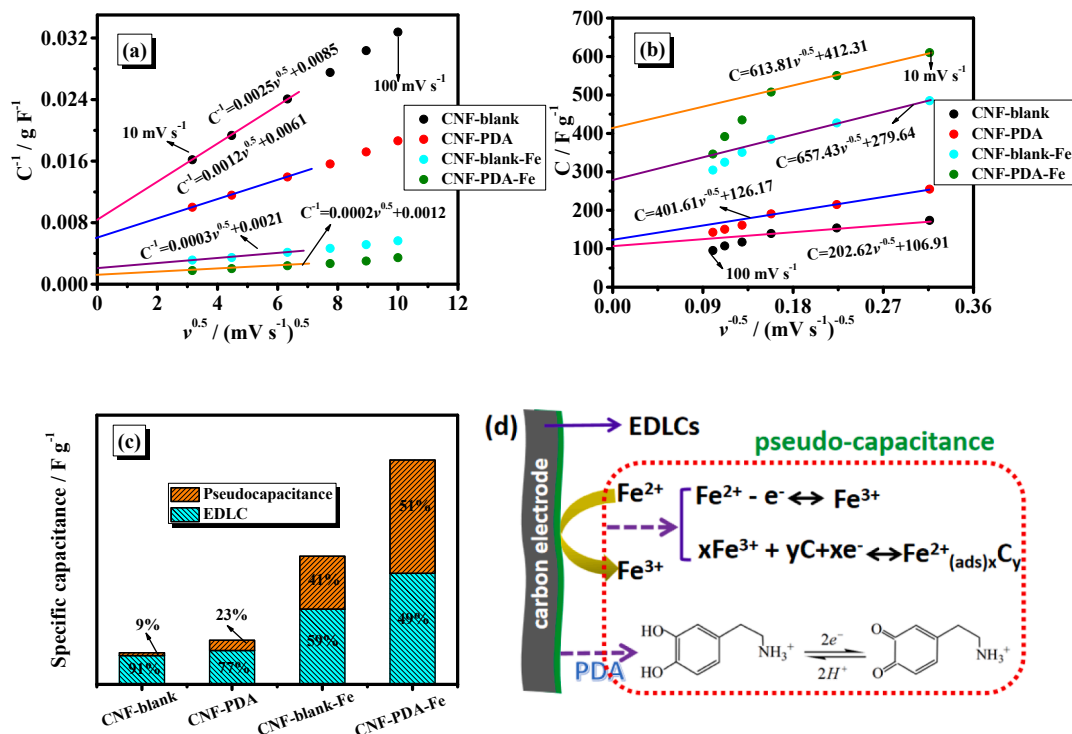


Fig. 7. The CNF-blank, CNF-PDA, CNF-blank-Fe, CNF-PDA-Fe samples: (a) Reciprocal curve of C (C^{-1}) against square root of scan rate ($v^{0.5}$); (b) Specific capacitance (C) against the reciprocal of square root of the scan rate ($v^{-0.5}$); (c) Contribution of EDLC and pseudo-capacitance; (d) Pseudo-reactions of Fe^{2+} and PDA.

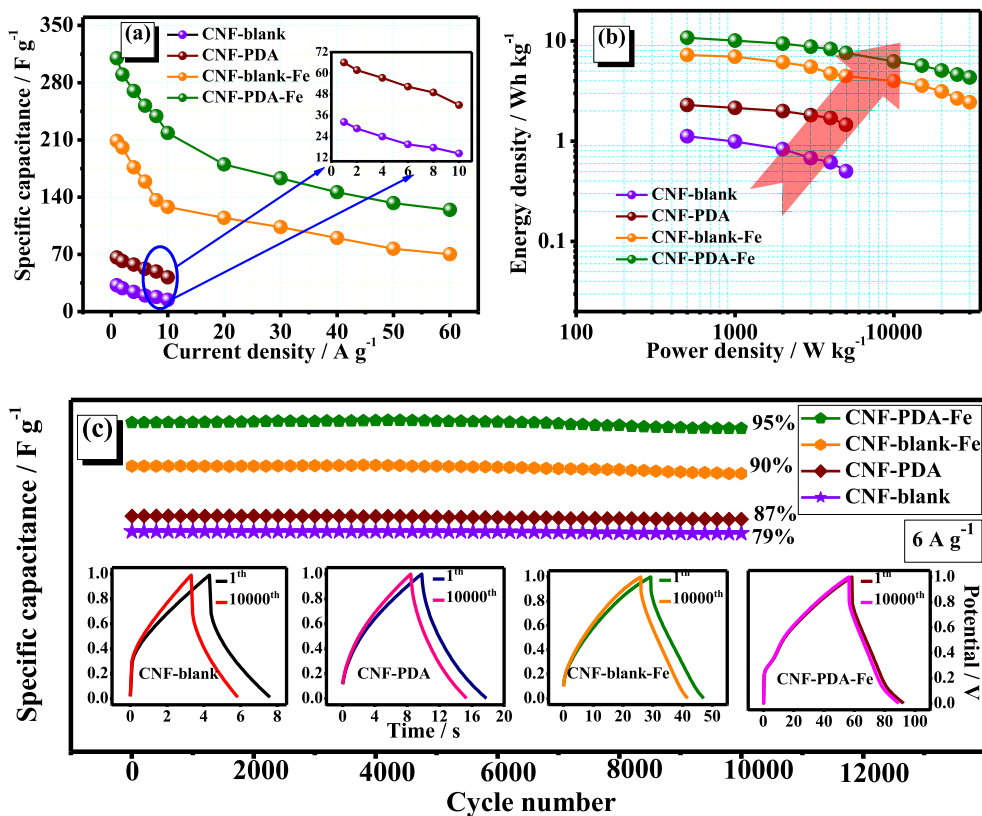


Fig. 8. The CNF-blank, CNF-PDA, CNF-blank-Fe, CNF-PDA-Fe samples when tested in a two-electrode configuration: (a) Specific capacitances at different current densities; (b) Ragone plots; (c) Cycling stability at 6 A g^{-1} .

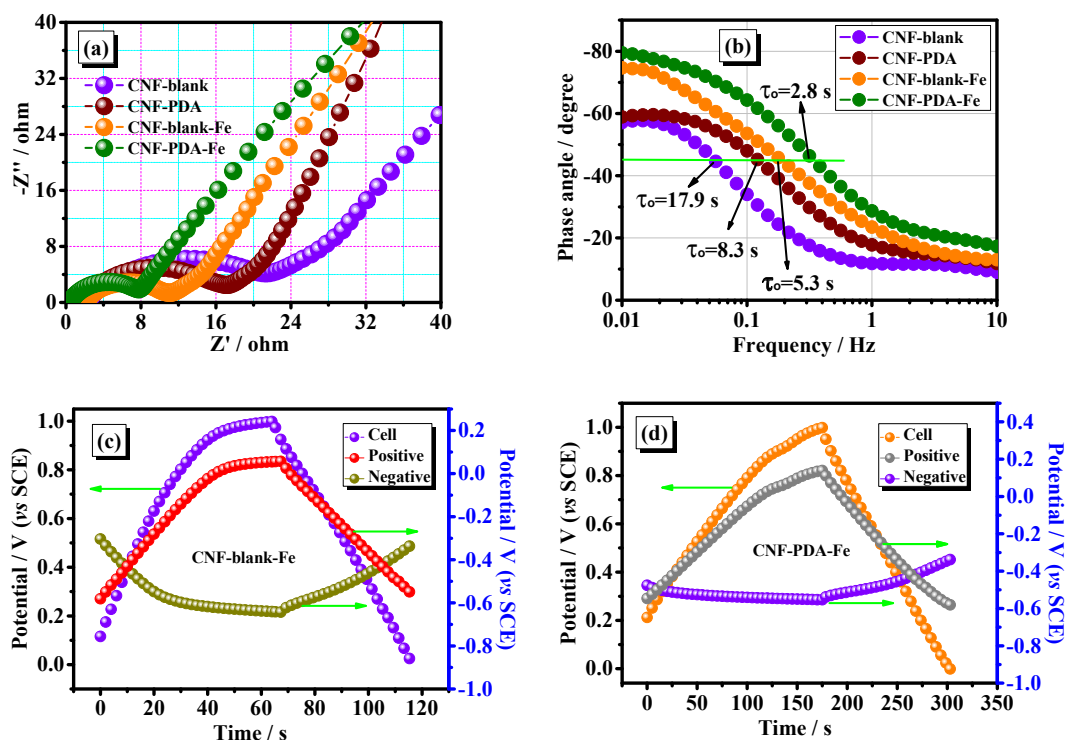


Fig. 9. The CNF-blank, CNF-PDA, CNF-blank-Fe, CNF-PDA-Fe samples when tested in a two-electrode configuration: (a) Nyquist plots; (b) Bode plots of the phase angle versus frequency; (c, d) GCD potential profiles for the positive electrode, negative electrode, and total two-electrode cell.

Table 2

Comparison of the performance of supercapacitors in two-electrode configuration.

Electrode materials	Electrolyte	Redox additive	Cs (F g ⁻¹)	Energy density (Wh kg ⁻¹)	Increase fold	Ref.
activated carbon	1 M KNO ₃	AQDS	128 at 2 A g ⁻¹	21.2 at 0.4 kW kg ⁻¹	2.04	[79]
activated carbon	PVA-KOH	KI	240 at 0.8 A g ⁻¹	7.8 at 1 kW kg ⁻¹	1.96	[80]
activated carbon	PVA-KOH	K ₃ [Fe(CN) ₆]	431 at 0.5 A g ⁻¹	57.94 at 1 kW kg ⁻¹	2.78	[81]
N/P-Carbon nanofiber	2 M H ₂ SO ₄	/	205 at 1 A g ⁻¹	7.76 at 1 kW kg ⁻¹	/	[19]
activated carbon	1 M H ₂ SO ₄	HQ	253 at 0.5 A g ⁻¹	8.8 at 0.25 kW kg ⁻¹	3.1	[69]
activated carbon	1 M H ₂ SO ₄	PMA	101 at 1 A g ⁻¹	3.5 at 0.5 kW kg ⁻¹	3.2	[82]
CNTs	PVA-Li ₂ SO ₄	BMIMBr	330 at 1 A g ⁻¹	43.1 at 0.2 kW kg ⁻¹	6.07	[83]
carbon nanosheets	1 M H ₂ SO ₄	HQ	72 at 2 A g ⁻¹	10.0 at 1 kW kg ⁻¹	1.64	[62]
activated carbon	PVA-H ₂ SO ₄	HQ	420 at 1 A g ⁻¹	11.0 at 1 kW kg ⁻¹	5.5	[84]
CNF-PDA-Fe	1 M H₂SO₄	Fe²⁺	219 at 10 A g⁻¹	10.07 at 1 kW kg⁻¹	10.17	this work

Note: 1. Increase fold refers to the increase in energy density; 2. AQDS is anthraquinone-2,7-disulphonate; 3. PMA is phosphomolybdic acid; 4. CNTs is carbon nanotubes; 5. BMIMBr is 1-butyl-3-methylimidazolium bromide.

(4) The surface coating of PDA can to large extent reduce the internal resistance of the electrode, which is conducive to obtaining an excellent energy density increase (10.17 times), far exceeding the performance of common redox additive.

The current strategy of PDA coating on carbon surfaces and the use of redox additives have developed an avenue for jointly improving the performance of supercapacitors and also can be easily extended to other systems.

CRediT authorship contribution statement

Zhong Jie Zhang: Investigation, Formal analysis, Writing - original draft. **Xiang Ying Chen:** Conceptualization, Writing - review & editing.

Declaration of Competing Interest

The authors declare that they have no known competing financial interests or personal relationships that could have appeared to influence the work reported in this paper.

Acknowledgements

This work was financially supported by National Natural Science Foundation of China (51602003), Startup Foundation for Doctors of Anhui University (J01003211), and Key Laboratory of Photovoltaic and Energy Conservation Materials, CAS (PECL2019KF001).

References

- Y. Zhai, Y. Dou, D. Zhao, P.F. Fulvio, R.T. Mayes, S. Dai, Carbon materials for chemical capacitive energy storage, *Adv. Mater.* 23 (2011) 4828–4850.
- M. Yang, Z. Zhou, Recent breakthroughs in supercapacitors boosted by nitrogen-rich porous carbon materials, *Adv. Sci.* 1600408 (2017).
- P. Simon, Y. Gogotsi, Capacitive energy storage in nanostructured carbonelectrolyte systems, *Acc. Chem. Res.* 46 (2013) 1094–1103.
- F. Béguin, V. Presser, A. Balducci, E. Frackowiak, Carbons and electrolytes for advanced supercapacitors, *Adv. Mater.* 26 (2014) 2219–2251.
- J. Wang, S. Kaskel, KOH activation of carbon-based materials for energy storage, *J. Mater. Chem.* 22 (2012) 23710–23725.
- F. Bonaccorso, L. Colombo, G. Yu, M. Stoller, V. Tozzini, A.C. Ferrari, R.S. Ruoff, V. Pellegrini, Graphene, related two-dimensional crystals, and hybrid systems for energy conversion and storage, *Science* 347 (2015) 1246501.
- Y. Zhu, S. Murali, M. Stoller, K.J. Ganesh, W. Cai, P.J. Ferreira, A. Pirkle, R.M. Wallace, K.A. Cygosh, M. Thommes, D. Su, E.A. Stach, R.S. Ruoff, Carbon-based supercapacitors produced by activation of graphene, *Science* 332 (2011) 1537–1541.
- Y. Xu, Z. Lin, X. Zhong, X. Huang, N.O. Weiss, Y. Huang, X. Duan, Holey graphene frameworks for highly efficient capacitive energy storage, *Nat. Commun.* 5 (2014) 4554.
- M.F.L. De Volder, S.H. Tawfik, R.H. Baughman, A. John Hart, Carbon nanotubes: present and future commercial applications, *Science* 339 (2013) 535–539.
- H. Pan, J. Li, Y. Peng, Carbon nanotubes for supercapacitor, *Nanoscale Res. Lett.* 5 (2010) 654–668.
- R.T.K. Baker, Carbon nanofibers, *Encyclopedia Mater.: Sci. Technol.* (2001) 932–941.
- S. Ma, Y. Wang, Z. Liu, M. Huang, H. Yang, Z. Xu, Preparation of carbon nanofiber with multilevel gradient porous structure for supercapacitor and CO₂ adsorption, *Chem. Eng. Sci.* 205 (2019) 181–189.
- Y. Gao, Z. Xiao, D. Kong, R. Iqbal, Q. Yang, L. Zhi, N. P co-doped hollow carbon nanofiber membranes with superior mass transfer property for trifunctional metal-free electrocatalysis, *Nano Energy* 64 (2019) 103879.
- Q. Jiang, X. Pang, S. Geng, Y. Zhao, X. Wang, H. Qin, B. Liu, J. Zhou, T. Zhou, Simultaneous cross-linking and pore-forming electrospun carbon nanofibers towards high capacitive performance, *Appl. Surface Sci.* 479 (2019) 128–136.
- V. Barranco, M.A. Lillo-Rodenas, A. Linares-Solano, A. Oya, F. Pico, J. Ibanez, F. Agullo-Rueda, J.M. Amarilla, J.M. Rojo, Amorphous carbon nanofibers and their activated carbon nanofibers as supercapacitor electrodes, *J. Phys. Chem. C* 114 (2010) 10302–10307.
- P.C. Banerjee, D.E. Lobo, T. Williams, M. Shaibani, M.R. Hill, M. Majumder, Graphitic carbon nanofiber growth from catalytic metal organic frameworks & their electrochemical double layer properties, *J. Mater. Chem. A* 5 (2017) 25338–25349.
- Z.Y. Wu, H.W. Liang, L.F. Chen, B.C. Hu, S.H. Yu, Bacterial cellulose: A robust platform for design of three dimensional carbon-based functional nanomaterials, *Acc. Chem. Res.* 49 (2016) 96–105.
- L. Chen, Z. Huang, H. Liang, W. Yao, Z. Yu, S. Yu, Flexible all-solid-state high-power supercapacitor fabricated with nitrogen-doped carbon nanofiber electrode material derived from bacterial cellulose, *Energy Environ. Sci.* 6 (2013) 3331–3338.
- L. Chen, Z. Huang, H. Liang, H. Gao, S. Yu, Three-dimensional heteroatom-doped carbon nanofiber networks derived from bacterial cellulose for Supercapacitors, *Adv. Funct. Mater.* 24 (2014) 5104–5111.
- C. Li, Y. Ding, B. Hu, Z. Wu, H. Gao, H. Liang, J. Chen, S. Yu, Temperature-invariant superelastic and fatigue resistant carbon nanofiber aerogels, *Adv. Mater.* 1904331 (2019).
- Z. Wu, C. Li, H. Liang, J. Chen, S. Yu, Ultralight, flexible, and fire-resistant carbon nanofiber aerogels from bacterial cellulose, *Angew. Chem. Int. Ed.* 52 (2013) 2925–2929.
- H. Liang, Z. Wu, L. Chen, C. Li, S. Yu, Bacterial cellulose derived nitrogen-doped carbon nanofiber aerogel: an efficient metal-free oxygen reduction electrocatalyst for zinc-air battery, *Nano Energy* 11 (2015) 366–376.
- A.S. Levitt, M. Alhabeib, C.B. Hatter, A. Sarycheva, G. Dion, Y. Gogotsi, Electrospun MXene/carbon nanofibers as supercapacitor electrodes, *J. Mater. Chem. A* 7 (2019) 269–277.
- Q. Meng, K. Qin, L. Ma, C. He, E. Liu, F. He, C. Shi, Q. Li, J. Li, N. Zhao, N-doped porous carbon nanofibers/porous silver network hybrid for high-rate supercapacitor electrode, *ACS Appl. Mater. Interfaces* 9 (2017) 30832–30839.
- H. Chen, T. Liu, J. Mou, W. Zhang, Z. Jiang, J. Liu, J. Huang, M. Liu, Free-standing N-self-doped carbon nanofiber aerogels for high-performance all-solid-state supercapacitors, *Nano Energy* 63 (2019) 103836.
- M. Zhi, A. Manivannan, F. Meng, N. Wu, Highly conductive electrospun carbon nanofiber/MnO₂ coaxial nano-cables for high energy and power density supercapacitors, *J. Power Sources* 208 (2012) 345–353.
- T. Kshetri, D. Tran, D. Nguyen, N. Kim, K. Lau, J. Lee, Ternary graphene-carbon nanofibers-carbon nanotubes structure for hybrid supercapacitor, *Chem. Eng. J.* 380 (2020) 122543.
- M. Yanilmaz, M. Dirican, A. Asiri, X. Zhang, Flexible polyaniline-carbon nanofiber supercapacitor electrodes, *J. Energy Storage* 24 (2019) 100766.
- J. Zhang, X. Zhang, Y. Zhou, S. Guo, K. Wang, Z. Liang, Q. Xu, Nitrogen-doped hierarchical porous carbon nanowhisker ensembles on carbon nanofiber for high-performance supercapacitors, *ACS Sustainable Chem. Eng.* 2 (2014) 1525–1533.
- M. Iguchi, S. Yamanaka, A. Budhiono, Bacterial cellulose—a masterpiece of nature's arts, *J. Mater. Sci.* 35 (2000) 261–270.
- F.G. Torres, J.J. Arroyo, O.P. Troncoso, Bacterial cellulose nanocomposites: An all-nano type of material, *Mater. Sci. Eng., C* 98 (2019) 1277–1293.
- P. Chen, S. Cho, H. Jin, Modification and applications of bacterial celluloses in polymer science, *Macromol. Res.* 18 (2010) 309–320.
- S. Wang, F. Jiang, X. Xu, Y. Kuang, K. Fu, E. Hitz, L. Hu, Super-strong, super-stiff macrofibers with aligned, long bacterial cellulose nanofibers, *Adv. Mater.* 29 (2017) 1702498.
- L. Huang, X. Du, S. Fan, G. Yang, H. Shao, D. Li, C. Cao, Y. Zhu, M. Zhu, Y. Zhang, Bacterial cellulose nanofibers promote stress and fidelity of 3D-printed silk based hydrogel scaffold with hierarchical pores, *Carbohydrate Poly.* 221 (2019) 146–156.
- Y. Liu, K. Ai, L. Lu, Polydopamine and its derivative materials: Synthesis and promising applications in energy, environmental, and biomedical fields, *Chem. Rev.* 114 (2014) 5057–5115.
- Y. Song, G. Ye, F. Wu, Z. Wang, S. Liu, M. Kopec, Z. Wang, J. Chen, J. Wang, K. Matyjaszewski, Bioinspired polydopamine (PDA) chemistry meets ordered mesoporous carbons (OMCs): a benign surface modification strategy for versatile functionalization, *Chem. Mater.* 28 (2016) 5013–5021.
- N.D.F. Vecchia, R. Avolio, M. Alfe, M.E. Errico, A. Napolitano, M. d'Ischia, Building-block diversity in polydopamine underpins a multifunctional eumelanin-type platform tunable through a quinone control point, *Adv. Funct. Mater.* 23 (2012) 1331–1340.
- M. Zhong, M. Wang, H. Liu, Y. Zhu, X. Chen, Z. Zhang, Hierarchically N/O-enriched nanoporous carbon for supercapacitor application: Simply adjusting the composition of deep eutectic solvent as well as the ratio with phenol-formaldehyde resin, *J. Power Sources* 438 (2019) 226982.
- A. Sadezky, H. Muckenhuber, H. Grothe, R. Niessner, U. Poshl, Raman microspectroscopy of soot and related carbonaceous materials: Spectral analysis and structural information, *Carbon* 43 (2005) 1731–1742.
- H. Liu, M. Wang, D. Zhai, X. Chen, Z. Zhang, Design and theoretical study of carbon-based supercapacitors especially exhibiting superior rate capability by the synergistic effect of nitrogen and phosphor dopants, *Carbon* 155 (2019) 223–232.
- R.A. Zangmeister, T.A. Morris, M.J. Tarlov, Characterization of polydopamine thin films deposited at short times by autoxidation of dopamine, *Langmuir* 29 (2013) 8619–8628.
- H. Luo, C. Gu, W. Zheng, F. Dai, X. Wang, Z. Zheng, Facile synthesis of novel size-controlled antibacterial hybrid spheres using silver nanoparticles loaded with polydopamine spheres, *RSC Adv.* 5 (2015) 13470–13477.
- B. Fei, B. Qian, Z. Yang, R. Wang, W. Liu, C. Mak, J. Xin, Coating carbon nanotubes by spontaneous oxidative polymerization of dopamine, *Carbon* 46 (2008) 1792–1828.
- J. Wang, K. Ren, H. Chang, S. Zhang, L. Jin, J. Ji, Facile fabrication of robust superhydrophobic multilayered film based on bioinspired poly(dopamine)-modified carbon nanotubes, *PCCP* 16 (2014) 2936–2943.
- T.I.T. Okpalugo, P. Papakonstantinou, H. Murphy, J. McLanghlin, N.M.D. Brown, High resolution XPS characterization of chemical functionalized MWCNTs and SWCNTs, *Carbon* 43 (2005) 153–161.
- Y. Nie, Q. Wang, X. Chen, Z. Zhang, Nitrogen and oxygen functionalized hollow carbon materials: the capacitive enhancement by simply incorporating novel redox additives into H₂SO₄ electrolyte, *J. Power Sources* 320 (2016) 140–152.
- J. Ryu, P.B. Messersmith, H. Lee, Polydopamine surface chemistry: a decade of discovery, *ACS Appl. Mater. Interfaces* 10 (2018) 7523–7540.
- G. Chen, T. Chen, K. Hou, W. Ma, M. Tebyetekerwa, Y. Cheng, W. Weng, M. Zhu, Robust, hydrophilic graphene/cellulose nanocrystal fiber-based electrode with high capacitive performance and conductivity, *Carbon* 127 (2018) 218–227.
- T. Guan, L. Shen, N. Bao, Hydrophilicity improvement of graphene fibers for high-performance flexible supercapacitor, *Ind. Eng. Chem. Res.* 58 (2019) 17338–17345.
- S. Dong, X. He, H. Zhang, X. Xie, M. Yu, C. Yu, N. Xiao, J. Qiu, Surface modification of biomass-derived hard carbon by grafting porous carbon nanosheets for high-performance supercapacitors, *J. Mater. Chem. A* 6 (2018) 15954–15960.
- M. Ryou, Y. Lee, J. Park, J. Choi, Mussel-inspired polydopamine-treated polyethylene separators for high-power Li-ion batteries, *Adv. Mater.* 23 (2011) 3066–3070.
- H. Lee, S.M. Dellatore, W.M. Miller, P.B. Messersmith, Mussel-inspired surface chemistry for multifunctional coatings, *Science* 318 (2007) 426–430.
- M. Wang, H. Liu, D. Zhai, X. Chen, Z. Zhang, In-situ synthesis of highly nitrogen, sulfur co-doped carbon nanosheets from melamine-formaldehyde-thiourea resin with improved cycling stability and energy density for supercapacitors, *J. Power Sources* 416 (2019) 79–88.
- X. Sun, W. Hu, D. Xu, X. Chen, P. Cui, Integration of redox additive in H₂SO₄ solution and the adjustment of potential windows for improving the capacitive performances of supercapacitors, *Ind. Eng. Chem. Res.* 56 (2017) 2433–2443.
- C. Singh, A. Paul, Physisorbed hydroquinone on activated charcoal as a supercapacitor: an application of proton-coupled electron transfer, *J. Phys. Chem. C* 119 (2015) 11382–11390.
- B. Mei, O. Munteshari, J. Lau, B. Dunn, L. Pilon, Physical interpretations of Nyquist plots for EDLC electrodes and devices, *J. Phys. Chem. C* 122 (2018) 194–206.
- M. Stoller, S. Park, Y. Zhu, J. An, R. Ruoff, Graphene-based ultracapacitors, *Nano Lett.* 8 (2008) 3498–3502.

- [58] J. Lee, P. Srimuk, S. Fleischmann, X. Su, T.A. Hatton, V. Presser, Redox-electrolytes for non-flow electrochemical energy storage: a critical review and best practice, *Prog. Mater. Sci.* 101 (2019) 46–89.
- [59] V. Augustyn, P. Simon, B. Dunn, Pseudocapacitive oxide materials for high-rate electrochemical energy storage, *Energy Environ. Sci.* 7 (2014) 1597–1614.
- [60] T. Liu, W. Pell, B.E. Conway, Behavior of molybdenum nitrides as materials for electrochemical capacitors: comparison with ruthenium oxide, *J. Electrochem. Soc.* 145 (1998) 1882–1888.
- [61] D. Xu, N. Sun, W. Hu, X. Chen, Carbon nanosheets-based supercapacitors: design of dual redox additives of 1, 4-dihydroxyanthraquinone and hydroquinone for improved performance, *J. Power Sources* 357 (2017) 107–116.
- [62] D. Xu, W. Hu, N. Sun, P. Cui, X. Chen, Redox additives of Na₂MoO₄ and KI: synergistic effect and the improved capacitive performances for carbon-based supercapacitors, *J. Power Sources* 341 (2017) 448–456.
- [63] Z. Zhang, J. Li, T. Huang, M. Liu, X. Chen, Large performance improvement of carbon-based supercapacitors using dual-redox additives phosphotungstic acid and potassium ferricyanide, *J. Alloy. Compd.* 768 (2018) 756–765.
- [64] Y. Tian, M. Liu, R. Che, R. Xue, L. Huang, Cooperative redox-active additives of anthraquinone-2,7-disulphonate and K₄Fe(CN)₆ for enhanced performance of active carbon-based capacitors, *J. Power Sources* 324 (2016) 334–341.
- [65] T. Li, C. Lin, A. Balamurugan, C. Kung, J. Wang, C. Hu, C. Wang, P. Chen, R. Vittal, K. Ho, Modification of glassy carbon electrode with a polymer/mediator composite and its application for the electrochemical detection of iodate, *Anal. Chim. Acta* 737 (2012) 55–63.
- [66] H. Wang, H. Yi, C. Zhu, X. Wang, H. Fan, Functionalized highly porous graphitic carbon fibers for high-rate supercapacitive electrodes, *Nano Energy* 13 (2015) 658–669.
- [67] S. Ardizzone, G. Fregonara, S. Trasatti, “Inner” and “outer” active surface of RuO₂ electrodes, *Electrochim. Acta* 35 (1990) 263–267.
- [68] D. Zhai, M. Wang, H. Liu, D. Wu, X. Chen, Z. Zhang, Integrating surface functionalization and redox additives to improve surface reactivity for high performance supercapacitors, *Electrochim. Acta* 323 (2019) 134810.
- [69] Y. He, Y. Zhang, X. Li, Z. Lv, X. Wang, Z. Liu, X. Huang, Capacitive mechanism of oxygen functional groups on carbon surface in supercapacitors, *Electrochim. Acta* 282 (2018) 618–625.
- [70] Y. Oh, J. Yoo, Y. Kim, J. Yoon, H. Yoon, J. Kim, S. Park, Oxygen functional groups and electrochemical capacitive behavior of incompletely reduced graphene oxides as a thin-film electrode of supercapacitor, *Electrochim. Acta* 116 (2014) 118–128.
- [71] H. Zhang, F. Zhang, S. Li, H. Li, A multilayer gold nanoparticle-polydopamine hybrid membrane-modified indium tin oxide electrode for selective sensing of dopamine in the presence of ascorbic acid, *Ionics* 23 (2017) 2475–2487.
- [72] Z. Zhang, S. Sun, Understanding the redox effects of amine and hydroxyl groups of *p*-aminophenol upon the capacitive performance in KOH and H₂SO₄ electrolyte, *J. Electroanal. Chem.* 778 (2016) 80–86.
- [73] Q. Li, K. Li, C. Sun, Y. Li, An investigation of Cu²⁺ and Fe²⁺ ions as active materials for electrochemical redox supercapacitors, *J. Electroanal. Chem.* 611 (2007) 43–50.
- [74] L. Sheng, L. Jiang, T. Wei, Z. Liu, Z. Fan, Spatial charge storage within honeycomb-carbon frameworks for ultrafast supercapacitors with high energy and power densities, *Adv. Energy Mater.* (2017) 1700668.
- [75] Taniya Purkait, Guneet Singh, Dinesh Kumar, Mandeep Singh, Ramendra Sundar Dey, High-performance flexible supercapacitors based on electrochemically tailored three-dimensional reduced graphene oxide networks, *Sci. Rep.* 8 (1) (2018), <https://doi.org/10.1038/s41598-017-18593-3>.
- [76] S. Chun, B. Evanko, X. Wang, D. Vonlanthen, X. Ji, G. Stucky, S. Boettcher, Design of aqueous redox-enhanced electrochemical capacitors with high specific energies and slow self-discharge, *Nat. Commun.* 6 (2015) 7818.
- [77] K. Jayaramulu, D.P. Dubal, B. Nagar, V. Ranc, O. Tomanec, M. Petr, K.K.R. Datta, R. Zboril, P. Gómez-Romero, R.A. Fischer, Ultrathin hierarchical porous carbon nanosheets for high-performance supercapacitors and redox electrolyte energy storage, *Adv. Mater.* 1705789 (2018).
- [78] Y. Tian, R. Xue, X. Zhou, Z. Liu, L. Huang, Double layer capacitor based on active carbon and its improved capacitive properties using redox additive electrolyte of anthraquinonedisulphonate, *Electrochim. Acta* 152 (2015) 135–139.
- [79] H. Yu, J. Wu, L. Fan, K. Xu, X. Zhong, Y. Lin, J. Lin, Improvement of the performance for quasi-solid-state supercapacitor by using PVA–KOH–KI polymer gel electrolyte, *Electrochim. Acta* 56 (2011) 6881–6886.
- [80] G. Ma, J. Li, K. Sun, H. Peng, J. Mu, Z. Lei, High performance solid-state supercapacitor with PVA-KOH-K₃[Fe(CN)₆] gel polymer as electrolyte and separator, *J. Power Sources* 256 (2014) 281–287.
- [81] Z. Zhang, Q. Song, W. He, P. Liu, Y. Xiao, J. Liang, X. Chen, Dual surface modification of carbon materials by polydopamine and phosphomolybdic acid for supercapacitor application, *Dalton Trans.* 48 (2019) 17321–17330.
- [82] L. Fan, Q. Tu, C. Geng, J. Huang, Y. Gu, J. Lin, Y. Huang, J. Wu, High energy density and low self-discharge of a quasi-solid-state supercapacitor with carbon nanotubes incorporated redox-active ionic liquid-based gel polymer electrolyte, *Electrochim. Acta* 331 (2020) 135425.
- [83] J. Zhong, L. Fan, X. Wu, J. Wu, G. Liu, J. Lin, M. Huang, Y. Wei, Improved energy density of quasi-solid-state supercapacitors using sandwich-type redox-active gel polymer electrolytes, *Electrochim. Acta* 166 (2015) 150–156.
- [84] D. Potphode, L. Sinha, P. Shirage, Redox additive enhanced capacitance: Multi-walled carbon nanotubes/polyaniline nanocomposite based symmetric supercapacitors for rapid charge storage, *Appl. Surface Sci.* 469 (2019) 162–172.